Nonlinearity Detection in Hyperspectral Images Using a Polynomial Post-Nonlinear Mixing Model

Yoann Altmann, *Student Member, IEEE*, Nicolas Dobigeon, *Member, IEEE*, and Jean-Yves Tourneret, *Senior Member, IEEE*

Abstract—This paper studies a nonlinear mixing model for hyperspectral image unmixing and nonlinearity detection. The proposed model assumes that the pixel reflectances are nonlinear functions of pure spectral components contaminated by an additive white Gaussian noise. These nonlinear functions are approximated by polynomials leading to a polynomial post-nonlinear mixing model. We have shown in a previous paper that the parameters involved in the resulting model can be estimated using least squares methods. A generalized likelihood ratio test based on the estimator of the nonlinearity parameter is proposed to decide whether a pixel of the image results from the commonly used linear mixing model or from a more general nonlinear mixing model. To compute the test statistic associated with the nonlinearity detection, we propose to approximate the variance of the estimated nonlinearity parameter by its constrained Cramér–Rao bound. The performance of the detection strategy is evaluated via simulations conducted on synthetic and real data. More precisely, synthetic data have been generated according to the standard linear mixing model and three nonlinear models from the literature. The real data investigated in this study are extracted from the Cuprite image, which shows that some minerals seem to be nonlinearly mixed in this image. Finally, it is interesting to note that the estimated abundance maps obtained with the post-nonlinear mixing model are in good agreement with results obtained in previous studies.

Index Terms—Constrained Cramér–Rao bound, nonlinearity detection, post-nonlinear mixing model (PPNMM), spectral unmixing (SU).

I. INTRODUCTION

ESTIMATING the macroscopic materials (endmembers) present in a hyperspectral image as well as their proportions (abundances) in each pixel of the scene is of prime interest when analyzing hyperspectral images. Most spectral unmixing (SU) strategies used for endmember and abundance estimation assume that the pixel reflectances are linear combinations of the endmembers [1]–[5]. However,

as explained in [6], the linear mixing model (LMM) can be inappropriate for some hyperspectral images, such as those containing sand, mineral mixtures, trees or vegetation areas. Nonlinear mixing models provide an interesting alternative for overcoming the inherent limitations of the LMM. Some nonlinear models have been proposed in the literature to handle specific kinds of nonlinearity. For instance, the bidirectional reflectance-based model studied in [7] has been introduced for intimate mixtures. The linear mixing model assumes that the components present in a given pixel are sitting side-by-side, leading to an observation that is the sum of the individual contribution of each material. Conversely, intimate mixtures occur when the photons are interacting with all the materials simultaneously, which can occur when the materials are not spatially distinguishable for instance. This kind of mixtures if often associated with sand or mineral areas. The bilinear models recently studied in [8]–[11] mainly focus on scattering effects, e.g., observed in vegetation areas. Radial basis function networks [12], [13] and kernel-based models studied in [14]–[17] have also been investigated for nonlinear SU.

This paper considers a specific nonlinear model studied in [18] for nonlinear SU and referred to as polynomial post-nonlinear mixing model (PPNMM). The PPNMM belongs to the wide class of post-nonlinear mixing models introduced in [19], [20] for source separation problems. It is a flexible generalization of the standard LMM that can accurately model many different nonlinearities. The PPNMM has the nice property to be characterized by few parameters. In particular, its nonlinearity part is governed by a single real parameter referred to as nonlinearity parameter. The parameters of the PPNMM can be estimated using standard Bayesian or least squares (LS) methods (see [18] for details).

Most existing unmixing algorithms can be decomposed into two steps. The first step is an endmember identification using all pixels of the image. In the last decades, many endmember extraction algorithms (EEAs) have been developed to identify the pure spectral components contained in a hyperspectral image. Geometrical approaches can be used to select the purest pixels of the image. The VCA algorithm [21] used in this paper belongs to this class of EEAs. This algorithm is known to be robust to the presence of weak nonlinearities in the image [11]. Other geometrical algorithms are based on the minimization of the volume containing the data, which allows the absence

of pure pixels to be mitigated. Finally, non-geometrical EEAs based on statistical approaches and sparse regression have also received a considerable attention in the literature. The reader is invited to consult [22] for a recent review of these methods. After estimating the endmembers, we propose to estimate the abundances, the nonlinearity parameter and the noise variance of the PPNMM using the subgradient method of [18].

This paper addresses the problem of determining whether an observed pixel of an hyperspectral image is a linear or nonlinear function of endmembers using the PPNMM. Note that the issue of nonlinearity detection in hyperspectral images has already been adressed in [23] to detected nonlinear areas in observed scenes using surrogate data. One of the most interesting properties of the PPNMM is that it generalizes the LMM thanks to a unique nonlinearity parameter whose value characterizes the nonlinearity in the considered pixel. In particular, when the nonlinearity parameter equals zero, the resulting mixing model is linear. Consequently, it seems natural to use this parameter for deriving new nonlinearity detectors. It is precisely the objective of this paper which is organized as follows. Section II introduces the PPNMM for hyperspectral image unmixing. Section III derives the statistical test for nonlinearity detection based on the parameter estimators provided by the LS unmixing procedure. Section IV studies the constrained Cramér–Rao lower bounds (CCRLBs) of the PPNMM parameter estimators. These bounds will be used to approximate variance of the nonlinearity parameter estimator yielding an approximated test statistics for nonlinearity detection. Simulation results conducted on synthetic data are finally shown in Section V.

II. POLYNOMIAL POST-NONLINEAR MIXING MODEL

This section introduces the nonlinear mixing model used for nonlinearity detection in hyperspectral images and the associated estimation algorithm.

A. PPNMM Model

The L-spectrum $\mathbf{y} = [y_1, \ldots, y_L]^T$ of a mixed pixel is generally defined as a nonlinear transformation $\boldsymbol{g}(\cdot)$ of a linear mixture of R endmembers $\mathbf{m}_1, \ldots, \mathbf{m}_R$ contaminated by additive noise

$$\mathbf{y} = \boldsymbol{g}\left(\sum_{r=1}^{R} a_r \mathbf{m}_r\right) + \mathbf{n} = \boldsymbol{g}(\mathbf{Ma}) + \mathbf{n} \qquad (1)$$

where $\mathbf{m}_r = [m_{r,1}, \ldots, m_{r,L}]^T$ is the spectrum of the rth material present in the scene, a_r is its corresponding proportion, R is the number of endmembers contained in the image and $\boldsymbol{g}(\cdot)$ is an appropriate nonlinear function. Moreover, L is the number of spectral bands and $\mathbf{n}$ is an additive independent and identically distributed (i.i.d) zero-mean Gaussian noise sequence with variance σ^2, denoted as $\mathbf{n} \sim \mathcal{N}(\mathbf{0}_L, \sigma^2 \mathbf{I}_L)$, where $\mathbf{I}_L$ is the $L \times L$ identity matrix. Note that the matrix and vector notations $\mathbf{M} = [\mathbf{m}_1, \ldots, \mathbf{m}_R]$ and $\mathbf{a} = [a_1, \ldots, a_R]^T$ have been used in the right hand side of (1).

Because of the lack of knowledge about the nonlinearity in (1), we proposed in [18] to approximate $\boldsymbol{g}(\cdot)$ using a second

order polynomial function $\boldsymbol{g}_b(\cdot)$ defined by

$$\boldsymbol{g}_b : [0, 1]^L \to \mathbb{R}^L$$
$$\boldsymbol{x} \mapsto \begin{bmatrix} x_1 + bx_1^2 \\ \vdots \\ x_L + bx_L^2 \end{bmatrix}$$

with $\boldsymbol{x} = [x_1, \ldots, x_L]^T$. An interesting property of the resulting PPNMM is that it reduces to the classical LMM for $b = 0$. Another motivation for using the PPNMM is the Weierstrass approximation theorem which states that any continuous function defined on a bounded interval can be uniformly approximated by a polynomial with any desired precision [24, p. 15]. As explained in [9], it is reasonable to consider polynomials with first and second order terms (since higher order terms can generally be neglected) which leads to the following mixing model (for a given pixel of the image)

$$\mathbf{y} = \boldsymbol{g}_b(\mathbf{Ma}) + \mathbf{n} = \mathbf{Ma} + b(\mathbf{Ma}) \odot (\mathbf{Ma}) + \mathbf{n} \qquad (2)$$

where $\odot$ denotes the Hadamard (term-by-term) product. Note that the resulting PPNMM includes bilinear terms such as those considered in [8]–[11]. However, the nonlinear terms are characterized by a single amplitude parameter b, which significantly simplifies the analysis.

Due to physical considerations, the abundance vector $\mathbf{a}$ satisfies the following positivity and sum-to-one constraints

$$\sum_{r=1}^{R} a_r = 1, \quad a_r \geq 0, \quad \forall r \in \{1, \ldots, R\}. \qquad (3)$$

Moreover, it has been shown in [18] that the PPNMM is general enough to handle a wide class of nonlinear models.

B. Parameter Estimation

The PPNMM parameters can be estimated by minimizing the following LS criterion

$$\begin{aligned} J(\mathbf{a}, b) &= \frac{1}{2} \left\| \mathbf{y} - \boldsymbol{g}_b(\mathbf{Ma}) \right\|^2 \\ &= \frac{1}{2} \left\| \mathbf{y} - \mathbf{Ma} - b(\mathbf{Ma}) \odot (\mathbf{Ma}) \right\|^2 \end{aligned} \qquad (4)$$

subject to the constraints (3), where $\|\mathbf{x}\| = \sqrt{\mathbf{x}^T \mathbf{x}}$ is the standard ℓ^2 norm. After estimating $\mathbf{a}$ and b, the noise variance σ^2 can be determined as follows

$$\hat{\sigma}^2 = \frac{1}{L} \left\| \mathbf{y} - \mathbf{M\hat{a}} - \hat{b}(\mathbf{M\hat{a}}) \odot (\mathbf{M\hat{a}}) \right\|^2. \qquad (5)$$

Since the additive noise vector $\mathbf{n}$ is i.i.d zero-mean and Gaussian, the resulting estimator of $\boldsymbol{\theta} = [\mathbf{a}^T, b, \sigma^2]^T$ is the maximum likelihood estimator (MLE) of $\boldsymbol{\theta}$, denoted as $\hat{\boldsymbol{\theta}}$. Consequently, the estimator $\hat{\boldsymbol{\theta}} = [\hat{\mathbf{a}}^T, \hat{b}, \hat{\sigma}^2]^T$ is asymptotically efficient and asymptotically distributed according to a Gaussian distribution [25, Chap. 7]. Note that the asymptotic region corresponds to $L \to \infty$. Since L is very large (some hundreds of spectral bands) for hyperspectral images,

the asymptotic region will be achieved in most practical applications.[1] The two LS algorithms considered in [18] (i.e., based on linearization and subgradient methods) for minimizing (4) subject to the constraints (3) have provided very similar performance. As a consequence, this paper will concentrate on one estimator only, namely the subgradient-based estimator. The next section derives a nonlinearity detector based on the MLE of the nonlinearity parameter.

III. NONLINEARITY DETECTION

As shown in Section II, the PPNMM allows the nonlinearity to be characterized by the parameter b for each pixel of the scene. An arbitrary threshold could be used to decide if the observed pixel is better modeled by the LMM or by a general nonlinear model defined by (2). However, it would be difficult to choose the appropriate threshold in order to guarantee a given probability of false alarm (PFA) or a given probability of detection (PD). In this section, we propose a statistical test for a pixel-by-pixel nonlinearity detection based on the distribution of $\hat{b}$. Based on the asymptotic properties of the MLE and on the large number of spectral bands available for a hyperspectral image, it makes sense to approximate the distribution of $\hat{b}$ by the following Gaussian distribution[2]

$$\hat{b} \sim \mathcal{N}\left(b, s^2\right) \tag{6}$$

where $s^2 \triangleq s^2(\mathbf{a}, b, \sigma^2)$ is the variance of the estimator $\hat{b}$. It is important to note that the variance of $\hat{b}$ is a function of the parameters $\mathbf{a}$, b and σ^2. Obviously, when the observation vector $\mathbf{y}$ results from the LMM (i.e., $b = 0$), then

$$\hat{b} \sim \mathcal{N}\left(0, s_0^2\right) \tag{7}$$

where $s_0^2 = s^2(\mathbf{a}, 0, \sigma^2)$. This interesting property can be used for testing the mixing model appropriate to the observation vector. The resulting nonlinearity detection problem can be considered as a two hypothesis testing problem, where the hypotheses are defined as

$$\begin{cases} H_0 : \mathbf{y} \text{ is distributed according to the LMM} \\ H_1 : \mathbf{y} \text{ is distributed according to the PPNMM.} \end{cases} \tag{8}$$

Hypothesis H_0 is characterized by $b = 0$ whereas nonlinear models (H_1) lead to $b \neq 0$. As a consequence, the two hypotheses in (8) can be rewritten as

$$\begin{cases} H_0 : \hat{b} \sim \mathcal{N}\left(0, s_0^2\right) \\ H_1 : \hat{b} \sim \mathcal{N}\left(b, s_1^2\right) \end{cases} \tag{9}$$

where $s_1^2 = s^2(\mathbf{a}, b, \sigma^2)$ and $b \neq 0$.

A. Known Parameters **a** and σ^2

For a given observation vector $\mathbf{y}$ and its corresponding estimated nonlinearity parameter $\hat{b}$, we propose to decide between hypotheses H_0 and H_1 using a classical generalized

[1] The asymptotic behavior of the considered MLEs will be discussed in Section V.
[2] This assumption will be validated in the simulation results.

likelihood ratio test (GLRT) for (9). Using (6) and (7), the GLRT consists of comparing the test statistic

$$\frac{\sup_{b} \; p(\hat{b}|H_1)}{p(\hat{b}|H_0)} \tag{10}$$

to an appropriate threshold, where $p(\hat{b}|H_0)$ (resp. $p(\hat{b}|H_1)$) is the probability density function of $\hat{b}$ under H_0 (resp. H_1). Obviously, $p(\hat{b}|H_1)$ is maximized for $b = \hat{b}$. Straightforward computations lead to the following test strategy

$$T = \frac{\hat{b}^2}{s_0^2} \underset{H_0}{\overset{H_1}{\gtrless}} \eta \tag{11}$$

where η is a threshold that is related to the test PFA as follows

$$\begin{aligned} P_{\text{FA}} &= \mathbb{P}\left[\frac{\hat{b}^2}{s_0^2} > \eta \middle| H_0\right] \\ &= 2\phi(-\sqrt{\eta}) \end{aligned} \tag{12}$$

where $\phi(\cdot)$ is the cumulative distribution function of the normalized Gaussian distribution. For a given value of b, the power of the test $P_{\text{D}}(b)$ can be computed as follows

$$P_{\text{D}}(b) = \mathbb{P}\left[\frac{\hat{b}^2}{s_0^2} > \eta \middle| H_1\right] = \mathbb{P}\left[\frac{\hat{b}^2}{s_0^2} > \eta \middle| b \neq 0\right]. \tag{13}$$

Straightforward computations lead to

$$P_{\text{D}}(b) = 1 + \phi\left(\frac{-s_0\sqrt{\eta} - b}{s_1}\right) - \phi\left(\frac{s_0\sqrt{\eta} - b}{s_1}\right). \tag{14}$$

It can be observed that for a given value of the threshold η, the probability of detection $P_{\text{D}}(b)$ is an increasing function of $|b|$, which is an intuitive result. In order to apply the detection strategy (11) and to compute the corresponding P_{FA} and $P_{\text{D}}(b)$, we need to know the parameters s_0 and s_1 whose determination is the objective of the next section.

B. Unknown Parameters **a** and σ^2

The test (11) assumes known parameters $\mathbf{a}$ and σ^2 to compute $s_0^2 = s^2(\mathbf{a}, 0, \sigma^2)$. However, these parameters are unknown in practical applications. To alleviate this problem, we propose to approximate the variance of $\hat{b}$ under H_0 by an appropriate estimator $\hat{s}_0^2$ leading to

$$\hat{T} = \frac{\hat{b}^2}{\hat{s}_0^2} \underset{H_0}{\overset{H_1}{\gtrless}} \eta^*. \tag{15}$$

More precisely, in order to build $\hat{s}_0^2$, we propose to use the constrained CRLB of $\boldsymbol{\theta} = [\mathbf{a}^T, b, \sigma^2]^T$ under hypothesis H_0 (i.e., $b = 0$) as explained in the next section.

IV. CONSTRAINED CRAMÉR–RAO BOUND

This section studies the constrained Cramér–Rao lower bound associated with any unbiased estimator $\hat{\boldsymbol{\theta}}$ of the parameter vector $\boldsymbol{\theta}$ involved in the PPNMM. Equation (2) shows that $\mathbf{y}|\mathbf{a}, b, \sigma^2 \sim \mathcal{N}\left(\boldsymbol{g}_b(\mathbf{Ma}), \sigma^2\mathbf{I}_L\right)$. As a consequence, the likelihood function of $\mathbf{y}$ is defined as

$$f(\mathbf{y}|\mathbf{a}, b, \sigma^2) = \left(\frac{1}{2\pi\sigma^2}\right)^{\frac{L}{2}} \exp\left(-\frac{\|\mathbf{y} - \boldsymbol{g}_b(\mathbf{Ma})\|^2}{2\sigma^2}\right). \tag{16}$$
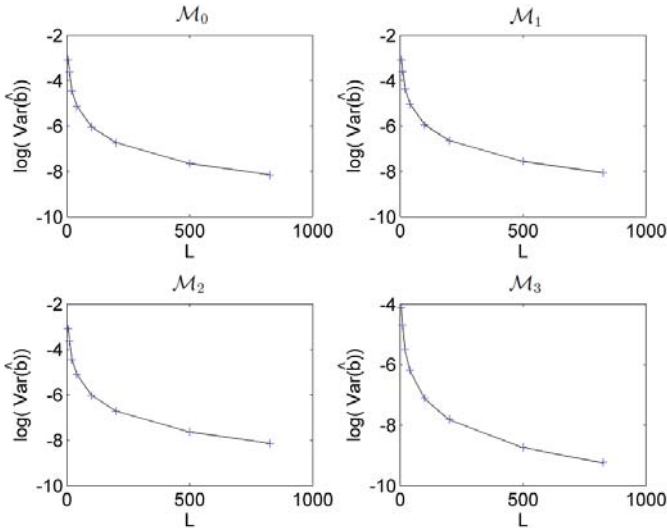
Fig. 1.   MSEs of the MLE (blue crosses) for the nonlinearity parameter b versus L compared with the CCRLBs (black lines).
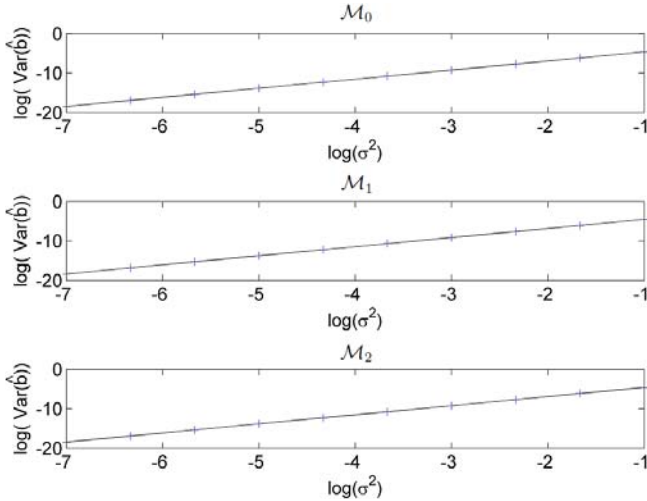

Fig. 2.   MSEs of the MLE (blue crosses) for the nonlinearity parameter b versus σ^2 compared with the CCRLBs (black lines).

The corresponding unconstrained CRLB for any unbiased estimator of $\boldsymbol{\theta}$ constructed from $\mathbf{y}$ is given by

$$\mathrm{CRLB}(\boldsymbol{\theta}) = \boldsymbol{J}_F^{-1} \qquad (17)$$

where $\boldsymbol{J}_F$ is the Fisher information matrix whose elements are[3]

$$[\boldsymbol{J}_F]_{i,j} = -\mathrm{E}_{\mathbf{y}|\boldsymbol{\theta}} \left[\frac{\partial^2 \ln f(\mathbf{y}|\boldsymbol{\theta})}{\partial \theta_i \partial \theta_j} \right] \quad i, j = 1, \dots, R+2.$$

However, the positivity and sum-to-one constraints (3) are not considered in this expression. Particularly, the sum-to-one constraint in (3) enforces the R-dimensional abundance vector $\mathbf{a}$ to belong to an $(R-1)$-dimensional subspace. This constraint can be considered by computing a reduced-rank Fisher matrix yielding a constrained Cramér–Rao lower bound (CCRLB). The CCRLB principles have been introduced in [26] for parameters satisfying equality and/or inequality constraints. The constraints for the abundance vector in (3) can be

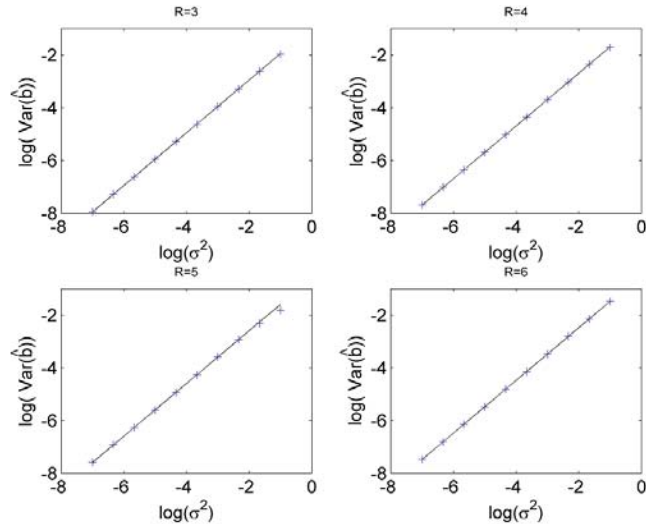[3]The Fisher information matrix $\boldsymbol{J}_F$ is derived in Appendix.

Fig. 3.   MSEs of the MLE (blue crosses) for the nonlinearity parameter b and $R = 3, 4, 5, 6$ versus σ^2 compared with the CCRLBs (black lines).

rewritten

$$u_{\boldsymbol{\theta}} = \begin{bmatrix} \mathbf{1}_R^T & 0 & 0 \end{bmatrix} \begin{bmatrix} \mathbf{a} \\ b \\ \sigma^2 \end{bmatrix} - 1 = \boldsymbol{c}^T \boldsymbol{\theta} - 1 = 0 \qquad (18)$$

and

$$\boldsymbol{v}_{\boldsymbol{\theta}} = \begin{bmatrix} -\mathbf{I}_R & \mathbf{0}_R & \mathbf{0}_R \end{bmatrix} \begin{bmatrix} \mathbf{a} \\ b \\ \sigma^2 \end{bmatrix} = \boldsymbol{A}\boldsymbol{\theta} \preceq \mathbf{0}_R \qquad (19)$$

where $\mathbf{1}_R$ is an $R \times 1$ vector of ones, $\boldsymbol{c} = [\mathbf{1}_R^T, 0, 0]^T$ is an $(R+2) \times 1$ vector, $\boldsymbol{A}$ is an $R \times (R+2)$ matrix, $u_{\boldsymbol{\theta}}$ is the equality constraint, $\boldsymbol{v}_{\boldsymbol{\theta}}$ is an $R \times 1$ pure inequality vector (see [26] for details) and $\preceq$ denotes the termwise inequality. Since the set of admissible $\boldsymbol{\theta}$ is an $(R+1)$-dimensional subset of $\mathbb{R}^{R+2}$, the CCRLB associated with the covariance matrix of any constrained unbiased estimator of $\boldsymbol{\theta}$ is given by [26]

$$\mathrm{CCRLB}(\boldsymbol{\theta}) = \boldsymbol{Q} \boldsymbol{J}_F^{-1} \qquad (20)$$

with

$$\boldsymbol{Q} = \mathbf{I}_{R+2} - \boldsymbol{J}_F^{-1} \nabla u_{\boldsymbol{\theta}} \left\{ \nabla u_{\boldsymbol{\theta}}^T \boldsymbol{J}_F^{-1} \nabla u_{\boldsymbol{\theta}} \right\} \nabla u_{\boldsymbol{\theta}}^T$$

where, from (18), $\nabla u_{\boldsymbol{\theta}} = \boldsymbol{c}$ is the gradient of $u_{\boldsymbol{\theta}}$. It is interesting to note that the CCRLB can be easily computed since this matrix results from simple operations applied on the unconstraint CRLB $\boldsymbol{J}_F^{-1}$ and the vector $\boldsymbol{c}$. Moreover, no arbitrary reparametrization is needed. The CCRLB of b is then given by the $(R+1)$th diagonal element of $\mathrm{CCRLB}(\boldsymbol{\theta})$ denoted as $\mathrm{CCRLB}(b; \mathbf{a}, \sigma^2)$. An estimator of the variance of $\hat{b}$ under hypothesis H_0 is required to compute the test statistic (15). We propose to estimate s_0^2 as follows

$$\hat{s}_0^2 = \mathrm{CCRLB}(0; \hat{\mathbf{a}}, \hat{\sigma}^2) \qquad (21)$$

where $\hat{\mathbf{a}}$ and $\hat{\sigma}^2$ are the MLEs of $\mathbf{a}$ and σ^2. The next sections study the performance of the nonlinearity detector defined by (15) for synthetic and real hyperspectral data.
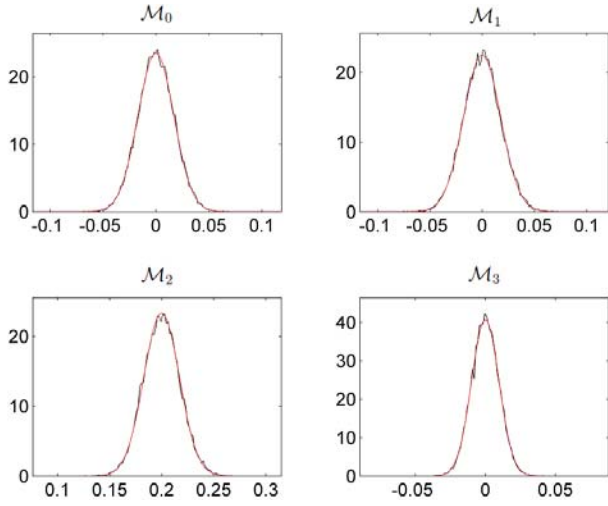
Fig. 4.   Histograms of $\hat{b}$ (black lines) and associated Gaussian distributions (red lines) for the four mixtures $\mathcal{M}_0$ to $\mathcal{M}_3$.

V. SYNTHETIC DATA

A. Estimation

The statistical test proposed in (15) assumes the efficiency and normality of the estimator $\hat{b}$ resulting from the unmixing procedure. We first propose to show that the asymptotic region in term of MLE efficiency is usually achieved in the hyperspectral imagery context [i.e., for large L and high signal to-noise ratio (SNR)]. Four different mixtures are considered to illustrate the estimator efficiency. These mixtures are composed of $R = 3$ materials (i.e., green grass, olive green paint and galvanized steel metal) whose endmember spectra, composed of $L = 826$ bands, have been extracted from the spectral libraries provided with the ENVI software [27]. The synthetic mixtures have been obtained using the following parameters[4]

Mixture $\mathcal{M}_0 : \mathbf{a} = [0.3, 0.6, 0.1]^T, b = 0, \sigma^2 = 3 \times 10^{-3}$
Mixture $\mathcal{M}_1 : \mathbf{a} = [0.5, 0.1, 0.4]^T, b = 0, \sigma^2 = 3 \times 10^{-3}$
Mixture $\mathcal{M}_2 : \mathbf{a} = [0.3, 0.6, 0.1]^T, b = 0.2, \sigma^2 = 3 \times 10^{-3}$
Mixture $\mathcal{M}_3 : \mathbf{a} = [0.3, 0.6, 0.1]^T, b = 0, \sigma^2 = 1 \times 10^{-3}$.

The efficiency of the proposed unmixing algorithm is evaluated by comparing the CCRLB presented in Section IV with the mean square errors (MSEs)

$$\text{MSE}(\hat{b}) = \frac{1}{N} \sum_{n=1}^{N} \left[\hat{b}^{(n)} - b^{(n)} \right]^2, \quad i = 1, \ldots, R+2 \quad (22)$$

associated with the nonlinearity parameter b, where N is the number of pixels to be unmixed and $\hat{b}^{(n)}$ is the estimated value of the nth actual parameter $b^{(n)}$.

Fig. 1 compares the MSEs of the subgradient-based estimator,[5] estimated with $N = 20000$ noise realizations, with the CCRLB versus the number of spectral bands (the number of spectral bands has been adjusted by a regular subsampling

[4]Note that $\mathcal{M}_1$, $\mathcal{M}_2$, and $\mathcal{M}_3$ have been obtained by changing $\mathbf{a}$, b, and σ^2 in $\mathcal{M}_0$, respectively.

[5]Similar results have been obtained using the linearization-based estimator and are reported in [28].

of the initial $L = 826$ bands). These results confirm the efficiency of the MLE for these four mixtures since the MSEs (crosses) are very close to the corresponding CCRLBs (continuous lines). Similarly, Fig. 2 compares the MSEs of the MLE (estimated with $N = 20000$ noise realizations and $L = 826$) with the CCRLB versus the noise variance σ^2 for the mixed pixels $\mathcal{M}_0$ to $\mathcal{M}_2$. These results show that the efficiency property is valid for any value of σ^2.

Fig. 3 compares the MSEs of the MLE (estimated with $N = 20000$ noise realizations and $L = 826$) with the CCRLB versus the noise variance σ^2 for $R = 3, 4, 5, 6$. The considered endmembers are the three materials presented above and construction concrete, micaceous loam and bare red brick. The synthetic mixtures have been obtained using the following parameters

$$R = 3 : \mathbf{a} = [0.3, 0.6, 0.1]^T, \quad b = 0.2$$
$$R = 4 : \mathbf{a} = [0.2, 0.3, 0.3, 0.2]^T, \quad b = 0.1$$
$$R = 5 : \mathbf{a} = [0.1, 0.15, 0.15, 0.2, 0.4]^T, \quad b = -0.2$$
$$R = 6 : \mathbf{a} = [0.15, 0.20, 0.25, 0.1, 0.1, 0.2]^T, \quad b = -0.1.$$

These results show that the efficiency assumption of Section III is valid for different values of R.

The asymptotic normality for the MLE of b is then investigated by considering the distributions of $\hat{b}$ for the four mixtures $\mathcal{M}_0$ to $\mathcal{M}_3$. The histograms of $\hat{b}$ estimated from $N = 20000$ Monte Carlo runs are depicted in Fig. 4. These results confirm that the distributions of the subgradient-based algorithm can be approximated by a Gaussian distribution whose mean is the actual parameter b and whose variance is given by the CCRLB.

B. Detection Performance

The performance of the proposed nonlinearity detection procedure can be measured by comparing the actual PFA (given by (12)) with the empirical PFA defined as

$$P_{\text{FA}}^{\text{emp}}(\eta) = \frac{1}{N} \sum_{n=1}^{N} d_n(\eta) \quad (23)$$

with

$$d_n(\eta) = \begin{cases} 0, & \text{if } T_n < \eta \\ 1, & \text{if } T_n > \eta \end{cases} \quad (24)$$

where N is the number of noisy realizations of a given mixture under H_0, η is the theoretical test threshold, T_n is the value of the test statistic for the nth noise realization and $d_n(\cdot)$ is its corresponding decision ($d_n(\cdot) = i$ means hypothesis H_i has been accepted with $i \in \{0, 1\}$). The actual PFA is also compared to its approximation obtained by approximating the CCRLB

$$P_{\text{FA}}^{\text{app}}(\eta) = \frac{1}{N} \sum_{n=1}^{N} \hat{d}_n(\eta) \quad (25)$$

where

$$\hat{d}_n(\eta) = \begin{cases} 0, & \text{if } \hat{T}_n < \eta \\ 1, & \text{if } \hat{T}_n > \eta. \end{cases} \quad (26)$$
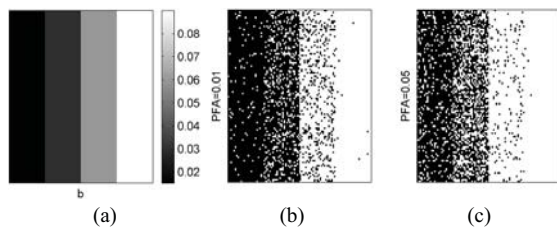
Fig. 5. (a) Actual values of b, and detection maps for (b) $P_{\text{FA}} = 0.01$ and (c) $P_{\text{FA}} = 0.05$, using the subgradient-based algorithm. Black pixels correspond to pixels detected as linearly mixed. White pixels correspond to pixels detected as nonlinearly mixed.

Fig. 5 compares P_{FA}, $P_{\text{FA}}^{\text{emp}}$ and $P_{\text{FA}}^{\text{appr}}$ as a function of the threshold η for $N = 20000$ noisy realizations of the mixture $\mathcal{M}_0$. These results first show that the theoretical and empirical PFAs coincide. Moreover, the CCRLB approximation proposed for the final test does not modify the performance in term of PFA.

Fig. 6 shows the test performance in term of receiver operating characteristics (ROCs) [29, p. 74-75] for $\mathbf{a} = [0.3, 0.6, 0.1]^T$ and $\sigma^2 = 3 \times 10^{-3}$ (SNR $= L^{-1}\sigma^{-2} \|\boldsymbol{g}_b(\mathbf{a})\|^2 \simeq 15$ dB). Four different values of b have been assumed under hypothesis H_1, i.e., $b = 5\sigma^2$, $b = 10\sigma^2$, $b = 15\sigma^2$ and $b = 20\sigma^2$. The theoretical ROCs are compared with the empirical and approximated ROCs, where the probabilities of detection are defined as

$$P_{\text{D}}^{\text{emp}}(\eta) = \frac{1}{N}\sum_{n=1}^{N} d_n(\eta) \qquad (27)$$

and

$$P_{\text{D}}^{\text{app}}(\eta^*) = \frac{1}{N}\sum_{n=1}^{N} \hat{d}_n(\eta) \qquad (28)$$

and where the data have been generated according to hypothesis H_1. These results show that the proposed test provides similar performance when compared to the original likelihood ratio test (assuming the actual parameters $\mathbf{a}$, b and σ^2 are known).

The performance of the proposed nonlinearity detector is also investigated by testing independently each pixel of a 100×100 synthetic image generated according to the PPNMM. The abundance vectors $\mathbf{a}_n$, $n = 1, \ldots, 10000$, have been randomly drawn from a uniform distribution in the simplex defined by the positivity and sum-to-one constraints. All pixels have been corrupted by an additive Gaussian noise of variance $\sigma^2 = 3 \times 10^{-3}$, corresponding to SNR $\simeq 15$ dB. The nonlinearity parameters have been chosen in the set $\{5\sigma^2, 10\sigma^2, 20\sigma^2, 30\sigma^2\}$, defining four different nonlinearity levels. Fig. 5 presents the actual nonlinearity parameters and the detection maps using the subgradient-based estimation procedure for $P_{\text{FA}} = 0.01$ and $P_{\text{FA}} = 0.05$. The white (resp. black) pixels are detected as nonlinearly (resp. linearly) distributed pixels. Note that similar results would be obtained when using the Taylor-based estimation procedure (see [28] for details).

The capacity of the PPNMM to detect various nonlinearities is then investigated by unmixing a 100×100 synthetic image generated according to four different mixing models. The $R = 3$ end members contained in this image have been
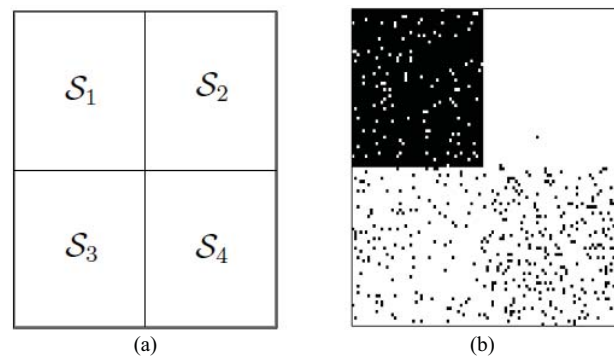

Fig. 6. (a) Actual location of the four sub-images S_1 (LMM), S_2 (FM), S_3 (GBM), and S_4 (PPNMM). (b) Associated detection map using the subgradient-based algorithm. Black pixels correspond to pixels detected as linearly mixed. White pixels correspond to pixels detected as nonlinearly mixed.

extracted from the spectral libraries provided with the ENVI software [27] (i.e., green grass, olive green paint and galvanized steel metal). The considered image is divided into four 50×50 sub-images as follows. The first synthetic sub-image S_1 has been generated using the standard linear mixing model (LMM). A second sub-image S_2 has been generated according to the bilinear mixing model introduced in [10], referred to as "Fan model" (FM). A third sub-image S_3 has been generated according to the generalized bilinear mixing model (GBM) recently introduced in [11], [30], whereas a fourth sub-image S_4 has been generated according to the proposed PPNMM. For each sub-image, the abundance uniform distribution in the admissible set defined by the positivity and sum-to-one constraints. All sub-images have been corrupted by an additive white Gaussian noise corresponding to SNR = 15 dB. The nonlinearity coefficients are uniformly drawn in the set $(0, 1)$ for the GBM and the parameter b has been generated uniformly in the set $(-0.3, 0.3)$ for the PPNMM. Fig. 6 shows the detection maps obtained with the GLRT for $P_{\text{FA}} = 0.05$. From this figure, it can be seen that the location of the nonlinear mixtures on the detection maps is straightforward. Note that for the GBM and the PPNMM, mixed pixels can be close to the simplex corresponding to the noise-free LMM and can be detected as linearly distributed pixels. Conversely, for the FM, only almost pure pixels are close to that simplex, leading to a larger number of pixels detected as nonlinear. This remark is illustrated in Fig. 7 which shows the location of the pixels detected as nonlinear in the 3-dimensional subspace spanned by the three dominant axes resulting from a principal component analysis.

VI. ANALYSIS OF REAL DATA

The performance of the proposed nonlinearity detector has been evaluated on a real hyperspectral image composed of $L = 189$ spectral bands. The selected scene has been extracted from the AVIRIS Cuprite image, acquired over a mining site in Nevada, in 1997. The geologic characteristics of the complete data have been described in [31]. The area of interest of size 190×250 is represented in Fig. 8 and has been previously studied in [21] to test the VCA algorithm with $R = 14$
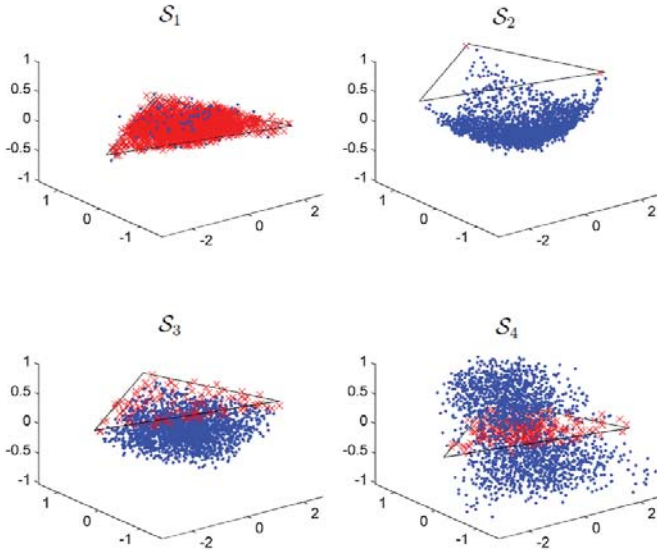
Fig. 7. Pixels detected as linear (red crosses) and nonlinear (blue dotted) for the four subimages S_1 (LMM), S_2 (FM), S_3 (GBM), and S_4 (PPNMM). Black lines depict the simplex corresponding to the noise-free case LMM.
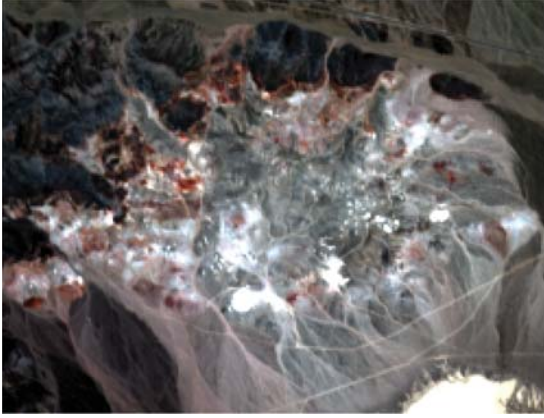

Fig. 8. AVIRIS image of 190×250 pixels extracted from Cuprite scene observed in composite natural colors.

endmembers. Therefore, in this experiment, the same number of endmembers has been extracted by VCA.

The subgradient-based estimator has been used to estimate the parameters of the PPNMM related to the analyzed image, i.e., the abundance vectors, the nonlinearity parameters and the noise variances associated with all image pixels[6]. Fig. 9 shows the abundance maps corresponding to the $R = 14$ components. The proportions of pure materials obtained with the PPNMM are in good agreement with those obtained with the LMM. However, the PPNMM has the advantage of providing additional information regarding the linearity or nonlinearity of endmember mixtures via the nonlinearity parameter b. Fig. 10 shows the estimated nonlinearity parameter map. Examples of decision maps associated with the subgradient-based estimator are also depicted in this figure. These decision maps have been obtained by applying the test (15) for all pixels of the image for two PFAs. Fig. 10 highlights some structures, e.g., the

[6]Similar results have been obtained using the linearization-based method. In the sequel of the paper, they are omitted for brevity but are reported in [28].

road is clearly identified at the top right corner, especially for $P_{FA} = 10^{-2}$. A spread nonlinear area is also detected (at the bottom left corner of the image). It can be noted from the classification map of [32] that this area is mainly composed of several kinds of Kaolinite. The proposed nonlinearity detector shows that nonlinear effects occur between the different kinds of Kaolinite in this area.

VII. Conclusion

A nonlinearity detector was presented for hyperspectral image analysis. This detector decided if a pixel of a hyperspectral image is a linear combination of endmembers or results from a general nonlinear mixture. It assumed that the hyperspectral image pixels are related to the endmembers by a polynomial post-nonlinear mixing model generalizing the widely used linear mixing model. A subgradient-based algorithm was used to estimate the model parameters. Constrained Cramér–Rao lower bounds were also derived for the PPNMM parameters. These bounds provide a reference in term of estimation variance for estimators satisfying the positivity and sum-to-one constraints of the abundances. The bound for the nonlinearity parameter was also used to approximate the variance of the nonlinearity detector investigated in this paper. Results obtained on synthetic and real images illustrated the accuracy of the polynomial post-nonlinear model for detecting nonlinearities in hyperspectral images.

It is interesting to note that the proposed nonlinearity detection strategy assumed fixed endmembers for all the pixels of the observed image. Accounting for the endmember variability is a problem that have recently received some attention in [3], [33], [34] and that might be considered for the proposed nonlinearity detector. This problem will be tackled in future works. The consideration of spatial correlation between pixels of the hyperspectral image to improve unmixing and detection results is also an interesting prospect.

Appendix

Fisher Information Matrix

The likelihood function of $\mathbf{y}$ can be expressed as

$$f(\mathbf{y}|\mathbf{a}, b, \sigma^2) = \left(\frac{1}{2\pi\sigma^2}\right)^{\frac{L}{2}} \exp\left(-\frac{\|\mathbf{y} - \boldsymbol{g}_b(\mathbf{Ma})\|^2}{2\sigma^2}\right)$$

where $\boldsymbol{g}_b(\mathbf{Ma}) = \mathbf{Ma} + b(\mathbf{Ma}) \odot (\mathbf{Ma})$ is the estimated spectrum of $\mathbf{y}$. The corresponding log-likelihood l can be written

$$l = \ln f(\mathbf{y}|\mathbf{a}, b, \sigma^2) = -\frac{L}{2}\ln(2\pi\sigma^2) - \frac{\|\mathbf{y} - \boldsymbol{g}_b(\mathbf{Ma})\|^2}{2\sigma^2}.$$

The partial derivatives of l with respect to the model parameters are

$$\frac{\partial l}{\partial a_r} = \frac{1}{2\sigma^2}\left[\mathbf{y} - \boldsymbol{g}_b(\mathbf{Ma})\right]^T \frac{\partial \boldsymbol{g}_b(\mathbf{Ma})}{\partial a_r}$$

$$\frac{\partial l}{\partial b} = \frac{1}{2\sigma^2}\left[\mathbf{y} - \boldsymbol{g}_b(\mathbf{Ma})\right]^T \frac{\partial \boldsymbol{g}_b(\mathbf{Ma})}{\partial b}$$

$$\frac{\partial l}{\sigma^2} = -\frac{L}{2\sigma^2} + \frac{\|\mathbf{y} - \boldsymbol{g}_b(\mathbf{Ma})\|^2}{2\sigma^4}.$$
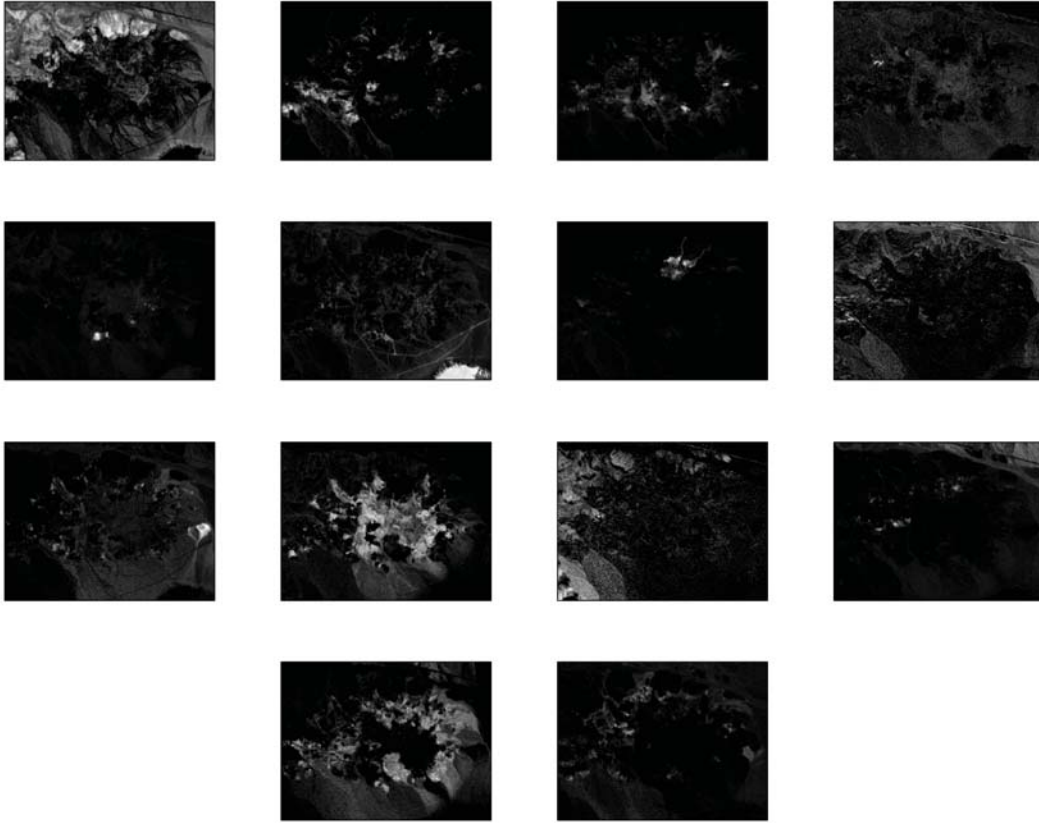
Fig. 9.   Fourteen abundance maps estimated with the subgradient algorithm for the Cuprite scene.

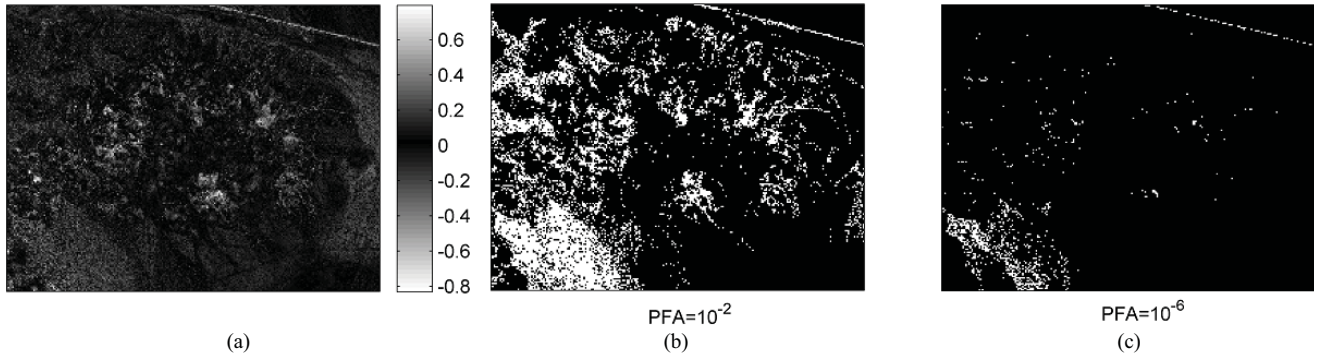(a)   (b)   (c)

Fig. 10.   (a) Map of $\hat{b}$ for the Cuprite scene. Associated detection map for (b) $P_{\mathrm{FA}} = 10^{-2}$ and (c) for $P_{\mathrm{FA}} = 10^{-6}$. Black pixels correspond to pixels detected as linearly mixed. White pixels correspond to pixels detected as nonlinearly mixed.

Straightforward computations lead to

$$-\mathrm{E}\left[\frac{\partial^2 l}{\partial a_i \partial a_j}\right] = -\mathrm{E}\left[\frac{\partial^2 l}{\partial a_j \partial a_i}\right]$$

$$= \frac{1}{2\sigma^2}\left(\frac{\partial \boldsymbol{g}_b(\mathbf{Ma})}{\partial a_i}\right)^T \frac{\partial \boldsymbol{g}_b(\mathbf{Ma})}{\partial a_j}$$

$$-\mathrm{E}\left[\frac{\partial^2 l}{\partial a_i \partial b}\right] = -\mathrm{E}\left[\frac{\partial^2 l}{\partial b \partial a_i}\right]$$

$$= \frac{1}{2\sigma^2}\left(\frac{\partial \boldsymbol{g}_b(\mathbf{Ma})}{\partial a_i}\right)^T \frac{\partial \boldsymbol{g}_b(\mathbf{Ma})}{\partial b}$$

$$-\mathrm{E}\left[\frac{\partial^2 l}{\partial^2 b}\right] = \frac{1}{2\sigma^2}\left(\frac{\partial \boldsymbol{g}_b(\mathbf{Ma})}{\partial b}\right)^T \frac{\partial \boldsymbol{g}_b(\mathbf{Ma})}{\partial b}$$

where

$$\frac{\partial \boldsymbol{g}_b(\mathbf{Ma})}{\partial a_r} = \mathbf{m}_r + 2b(\mathbf{Ma}) \odot \mathbf{m}_r$$

$$\frac{\partial \boldsymbol{g}_b(\mathbf{Ma})}{\partial b} = (\mathbf{Ma}) \odot (\mathbf{Ma}).$$

It can be easily shown that

$$-\mathrm{E}\left[\frac{\partial^2 l}{\partial a_i \partial \sigma^2}\right] = -\mathrm{E}\left[\frac{\partial^2 l}{\partial \sigma^2 \partial a_i}\right] = 0$$

$$-\mathrm{E}\left[\frac{\partial^2 l}{\partial b \partial \sigma^2}\right] = -\mathrm{E}\left[\frac{\partial^2 l}{\partial \sigma^2 \partial b}\right] = 0$$

$$-\mathrm{E}\left[\frac{\partial^2 l}{\partial^2 \sigma^2}\right] = \frac{L}{2\sigma^4}.$$

References

[1] M. Craig, "Minimum-volume transforms for remotely sensed data," *IEEE Trans. Geosci. Remote Sensing*, vol. 32, no. 3, pp. 542–552, May 1994.

[2] D. C. Heinz and C.-I Chang, "Fully constrained least squares linear spectral mixture analysis method for material quantification in hyperspectral imagery," *IEEE Trans. Geosci. Remote Sensing*, vol. 39, no. 3, pp. 529–545, Mar. 2001.

[3] O. Eches, N. Dobigeon, C. Mailhes, and J.-Y. Tourneret, "Bayesian estimation of linear mixtures using the normal compositional model. Application to hyperspectral imagery," *IEEE Trans. Image Process.*, vol. 19, no. 6, pp. 1403–1413, Jun. 2010.

[4] L. Miao, H. Qi, and H. Szu, "A maximum entropy approach to unsupervised mixed-pixel decomposition," *IEEE Trans. Image Process.*, vol. 16, no. 4, pp. 1008–1021, Apr. 2007.

[5] Z. Yang, G. Zhou, S. Xie, S. Ding, J.-M. Yang, and J. Zhang, "Blind spectral unmixing based on sparse nonnegative matrix factorization," *IEEE Trans. Image Process.*, vol. 20, no. 4, pp. 1112–1125, Apr. 2011.

[6] N. Keshava and J. F. Mustard, "Spectral unmixing," *IEEE Signal Process. Mag.*, vol. 19, no. 1, pp. 44–57, Jan. 2002.

[7] B. W. Hapke, "Bidirectional reflectance spectroscopy. I. Theory," *J. Geophys. Res.*, vol. 86, pp. 3039–3054, Apr. 1981.

[8] B. Somers, K. Cools, S. Delalieux, J. Stuckens, D. V. der Zande, W. W. Verstraeten, and P. Coppin, "Nonlinear hyperspectral mixture analysis for tree cover estimates in orchards," *Remote Sensing Environ.*, vol. 113, no. 6, pp. 1183–1193, 2009.

[9] J. M. P. Nascimento and J. M. Bioucas-Dias, "Nonlinear mixture model for hyperspectral unmixing," *Proc. SPIE*, vol. 1, pp. 74770I-1–74770I-8, Sep. 2009.

[10] W. Fan, B. Hu, J. Miller, and M. Li, "Comparative study between a new nonlinear model and common linear model for analysing laboratory simulated-forest hyperspectral data," *Remote Sensing Environ.*, vol. 30, no. 11, pp. 2951–2962, Jun. 2009.

[11] A. Halimi, Y. Altmann, N. Dobigeon, and J.-Y. Tourneret, "Nonlinear unmixing of hyperspectral images using a generalized bilinear model," *IEEE Trans. Geosci. Remote Sensing*, vol. 49, no. 11, pp. 4153–4162, Nov. 2011.

[12] K. J. Guilfoyle, M. L. Althouse, and C.-I Chang, "A quantitative and comparative analysis of linear and nonlinear spectral mixture models using radial basis function neural networks," *IEEE Geosci. Remote Sensing*, vol. 39, no. 8, pp. 2314–2318, Aug. 2001.

[13] Y. Altmann, N. Dobigeon, S. McLaughlin, and J.-Y. Tourneret, "Nonlinear unmixing of hyperspectral images using radial basis functions and orthogonal least squares," in *Proc. IEEE Int. Conf. Geosci. Remote Sensing*, Jul. 2011, pp. 1151–1154.

[14] J. Broadwater, R. Chellappa, A. Banerjee, and P. Burlina, "Kernel fully constrained least squares abundance estimates," in *Proc. IEEE Int. Conf. Geosci. Remote Sensing*, Jul. 2007, pp. 4041–4044.

[15] K.-H. Liu, E. Wong, and C.-I Chang, "Kernel-based linear spectral mixture analysis for hyperspectral image classification," in *Proc. IEEE GRSS Workshop Hyperspectral Image Signal Process., Evol. Remote Sensing*, Aug. 2009, pp. 1–4.

[16] J. Broadwater and A. Banerjee, "Mapping intimate mixtures using an adaptive kernel-based technique," in *Proc. IEEE GRSS Workshop Hyperspectral Image Signal Process., Evol. Remote Sensing*, Jun. 2011, pp. 1–4.

[17] J. Chen, C. Richard, and P. Honeine, "A novel kernel-based nonlinear unmixing scheme of hyperspectral images," in *Proc. Asilomar Conf. Signals, Syst., Comput.*, Nov. 2011, pp. 1898–1902.

[18] Y. Altmann, A. Halimi, N. Dobigeon, and J.-Y. Tourneret, "Supervised nonlinear spectral unmixing using a post-nonlinear mixing model for hyperspectral imagery," *IEEE Trans. Image Process.*, vol. 21, no. 6, pp. 3017–3025, Jun. 2012.

[19] C. Jutten and J. Karhunen, "Advances in nonlinear blind source separation," in *Proc. 4th Int. Symp. Independ. Comp. Anal. Blind Signal Separat.*, Nara, Japan, Apr. 2003, pp. 245–256.

[20] M. Babaie-Zadeh, C. Jutten, and K. Nayebi, "Separating convolutive post non-linear mixtures," in *Proc. 3rd Workshop Independ. Comp. Anal. Signal Separat.*, San Diego, CA, 2001, pp. 138–143.

[21] J. M. Nascimento and J. M. Bioucas-Dias, "Vertex component analysis: A fast algorithm to unmix hyperspectral data," *IEEE Trans. Geosci. Remote Sensing*, vol. 43, no. 4, pp. 898–910, Apr. 2005.

[22] M. Parente and A. Plaza, "Survey of geometric and statistical unmixing algorithms for hyperspectral images," in *Proc. IEEE GRSS Workshop Hyperspectral Image Signal Process., Evol. Remote Sensing*, Reykjavík, Iceland, 2010, pp. 1–4.

[23] T. Han and D. Goodenough, "Investigation of nonlinearity in hyperspectral imagery using surrogate data methods," *IEEE Trans. Geosci. Remote Sensing*, vol. 46, no. 10, pp. 2840–2847, Oct. 2008.

[24] V. J. Mathews and G. L. Sicuranza, *Polynomial Signal Processing*. New York: Wiley, 2000.

[25] S. M. Kay, *Fundamentals of Statistical Signal Processing: Estimation Theory*. Englewood Cliffs, NJ: Prentice-Hall, 1993.

[26] J. Gorman and A. Hero, "Lower bounds for parametric estimation with constraints," *IEEE Trans. Inf. Theory*, vol. 36, no. 6, pp. 1285–1301, Nov. 1990.

[27] *ENVI User's Guide Version 4.0*, Research Systems Inc., Boulder, CO, Sep. 2003.

[28] Y. Altmann, N. Dobigeon, and J.-Y. Tourneret, "Nonlinearity detection in hyperspectral images using a polynomial post-nonlinear mixing model," IRIT/INP-ENSEEIHT, Univ. Toulouse, Toulouse, France, Tech. Rep., Dec. 2011.

[29] S. M. Kay, *Fundamentals of Statistical Signal Processing: Detection Theory*. Englewood Cliffs, NJ: Prentice-Hall, 1998.

[30] A. Halimi, Y. Altmann, N. Dobigeon, and J.-Y. Tourneret, "Unmixing hyperspectral images using a generalized bilinear model," in *Proc. IEEE Int. Conf. Geosci. Remote Sensing*, Jul. 2011, pp. 1886–1889.

[31] R. N. Clark, G. A. Swayze, K. E. Livo, R. F. Kokaly, S. J. Sutley, J. B. Dalton, R. R. McDougal, and C. A. Gent, "Imaging spectroscopy: Earth and planetary remote sensing with the USGS Tetracorder and expert systems," *J. Geophys. Res.*, vol. 108, no. E12, pp. 5-1–5-44, Dec. 2003.

[32] R. N. Clark, G. A. Swayze, and A. Gallagher, "Mapping minerals with imaging spectroscopy," *U.S. Geological Survey Off. Mineral Resour. Bulletin*, vol. 2039, pp. 141–150, Mar. 1993.

[33] B. Somers, G. P. Asner, L. Tits, and P. Coppin, "Endmember variability in spectral mixture analysis: A review," *Remote Sensing Environ.*, vol. 115, no. 7, pp. 1603–1616, 2011.

[34] A. Zare, P. Gader, T. Allgire, D. Drashnikov, and R. Close, "Bootstrapping for piece-wise convex endmember distribution detection," in *Proc. IEEE GRSS Workshop Hyperspectral Image Signal Process., Evol. Remote Sensing*, May 2012, pp. 1–4.

Yoann Altmann (S'10) was born in Toulouse, France, in 1987. He received the Eng. degree in electrical engineering from the ENSEEIHT, Toulouse, and the M.Sc. degree in signal processing from the National Polytechnic Institute of Toulouse, Toulouse, both in 2010. He is currently pursuing the Ph.D. degree with the Signal and Communication Group, IRIT Laboratory, Toulouse.

Nicolas Dobigeon (S'05–M'08) was born in Angoulême, France, in 1981. He received the Eng. degree in electrical engineering from ENSEEIHT, Toulouse, France, in 2004, and the M.Sc. and Ph.D. degrees in signal processing from the National Polytechnic Institute of Toulouse, in 2004 and 2007, respectively.

He was a Post-Doctoral Research Associate with the Department of Electrical Engineering and Computer Science, University of Michigan, Ann Arbor, from 2007 to 2008. Since 2008, he has been an Assistant Professor with the National Polytechnic Institute of Toulouse (ENSEEIHT, University of Toulouse), within the Signal and Communication Group of the IRIT Laboratory. His current research interests include statistical signal and image processing, with a particular interest in Bayesian inverse problems with applications to remote sensing, biomedical imaging and genomics.

Jean-Yves Tourneret (SM'08) received the Ingénieur degree in electrical engineering from the École Nationale Supérieure d' Électronique, d' Électrotechnique, d'Informatique, d'Hydraulique, et des Télécommunications (ENSEEIHT), Toulouse, France, in 1989, and the Ph.D. degree from National Polytechnic Institute, Toulouse, in 1992.

He is currently a Professor with the University of Toulouse (ENSEEIHT) and a Member of the IRIT Laboratory (UMR 5505 of the CNRS). His current research interests include statistical signal processing with a particular interest to Bayesian methods and Markov chain Monte Carlo (MCMC) algorithms.

Prof. Tourneret was the Program Chair of the European Conference on Signal Processing (EUSIPCO), held in Toulouse in 2002. He was also a member of the Organizing Committee for the International Conference ICASSP'06 in Toulouse in 2006. He has been a member of different technical committees, including the Signal Processing Theory and Methods (SPTM) Committee of the IEEE Signal Processing Society (2001 -2007 and 2010 -present). He has been serving as an Associate Editor for the IEEE TRANSACTIONS ON SIGNAL PROCESSING from 2008 to 2011.